Engineering Geology 223 (2017) 48–58

Contents lists available at ScienceDirect

Engineering Geology

journal homepage: www.elsevier.com/locate/enggeo

Modelling of compacted bentonite swelling accounting for salinity effects

Vicente Navarro[a,*], Ángel Yustres[a], Laura Asensio[a], Gema De la Morena[a], Jesús González-Arteaga[a], Teemu Laurila[b], Xavier Pintado[b]

[a] Geoenvironmental Group, Civil Engineering Department, University of Castilla-La Mancha, Avda. Camilo José Cela s/n, 13071 Ciudad Real, Spain
[b] B + Tech Oy, Laulukuja 4, 00420 Helsinki, Finland

ARTICLE INFO

Keywords:
Bentonite swelling
Salinity effects
Electrochemical potential
Destructuration
Modelling

ABSTRACT

This paper presents a formulation to incorporate the influence of water salinity on the swelling behaviour of a MX-80 bentonite into previously developed hydro-mechanical models that can reproduce swelling under dilute conditions. The effects of salinity on macro- and microstructural water chemical potentials were introduced. In addition, a description of solute transport was included to characterise the evolution of the system's salinity. A simplified geochemical model was adopted to idealise the geochemical complexity of bentonite. In addition, the modelling of the destructuration process that occurs during swelling was modified to account for the effect of salinity. The formulation was implemented in a multiphysics partial differential equation finite element solver, and the numerical model was used to simulate several vertical free swelling tests with feed water of different salt contents (deionised, 10, 35 and 70 g/L). The results demonstrate that even though the model can be developed further, it represents a significant improvement over models that do not account for the effects of salinity.

1. Introduction

The highly expansive behaviour and low hydraulic conductivity of bentonites make them good sealing materials for engineered barrier systems in deep geological repositories for spent nuclear fuel. The operation conditions of these systems will vary widely throughout their useful life. It is therefore essential to have a bentonite stress-strain constitutive model that is capable of estimating its long term behaviour. The characterisation of the hydration and swelling of bentonite is particularly important because these properties define its the ability to seal gaps (natural or associated with the construction process) that may exist in engineered barrier systems.

Given the importance of this matter, a significant amount of research has focused on bentonite hydration (see for example the contributions in Tournassat et al., 2015). Most of these studies assume a hierarchical idealisation of the clay fabric (Yong, 1999). However, even in compacted bentonites, the stacking of clay layers to form particles is irregular, which generates micro-voids inside the particles (Cases et al., 1992). Furthermore, the particles split into smaller ones along wetting paths Saiyouri et al. (2004) suggested that swelling is essentially a process of subdivision of the clay particles and not a homogeneous increase in the distance between the layers. Similar processes occur in the particle aggregates (Salles et al., 2009). As a result, the internal topology of bentonite is irregular, and both the particles and the aggregates they form should be considered dynamic functional structures that evolve throughout the hydration process. This evolution conditions the process itself. Swelling is a non-linear (Wang et al., 2015) complex process in which "competition" for water occurs between the hydration of cations, the hydration of the charged surface of the clay, the separation of particles, the adsorption in the intra-aggregate pores (microporosity), the hydration of the inter-aggregate space (macroporosity) and diffuse double layer development (Salles et al., 2009).

Despite significant advances in upscaling techniques based on the Homogenization Theory (Marry and Rotenberg, 2015), the complexity of these phenomena still makes it difficult to define a macroscopic model that will solve engineering-scale problems (i.e., behaviour of the repository) through the integration of microscopic processes. To obtain a macroscopic model, it is necessary to introduce simplifying hypotheses that avoid characterising some of the processes that occur at a microscopic level. The most frequent simplification strategy for compacted bentonite is to consider it as a double porosity medium (e.g., Alonso et al., 1999; Mašín, 2013). This approach is based on the bimodal distribution of porosity observed when the material is analysed using porosimetry techniques (Romero et al., 1999) to identify the macrostructural porosity with the space between the bentonite particle aggregates, and the microstructural porosity with their internal voids. While this fabric evolves throughout the hydration process as a result of

* Corresponding author.
E-mail address: vicente.navarro@uclm.es (V. Navarro).

http://dx.doi.org/10.1016/j.enggeo.2017.04.016
Received 16 November 2016; Received in revised form 16 March 2017; Accepted 9 April 2017
Available online 22 April 2017
0013-7952/

the previously described microscopic processes (Burton et al., 2015), the double porosity models satisfactorily reproduce the macroscopic effects of these changes on deformability and flow (Gens and Alonso, 1992).

Hydro-mechanical models have typically been used for dilute conditions. However, these models must be modified to describe the response of bentonites to variations in salinity. This topic is important for deep geological repositories, where significant changes in the chemistry of the surrounding groundwater and thus of the interstitial porewater will take place (Hellä et al., 2014). Many experimental studies have been conducted to characterise the effect of porewater salinity on the hydro-mechanical behaviour of bentonite. These studies have confirmed that the swelling pressure decreases when the porewater's ionic strength increases (Karnland et al., 2005; Zhu et al., 2013). Alawaji (1999) showed in swelling tests that the initial strain velocity increases and the swelling capacity decreases as the concentrations increase. In addition, since the seminal work of Quirk and Schofield (1955), several authors have shown that the hydraulic conductivity of bentonites increases when they are saturated with solutions of increasing salinity (Zhu et al., 2013).

To introduce these processes into constitutive models, simplified models of the geochemical configuration of the clay have been adopted (see Guimarães et al., 2013, for instance), which often assume a system that is composed of two basic cations (usually Na^+ and Ca^{2+}) and a single anion (typically, Cl^-). This has allowed researchers to characterise the response of the material to simple "chemical loads" and to better understand the importance of hydro-mechanical-chemical coupling on the deformational behaviour of bentonites. Currently, thermo-hydro-mechanical and chemical models are being developed with a broader geochemical basis (Zheng et al., 2015).

However, those formulations are primarily aimed at confined conditions and not at free swelling conditions that may occur in the presence of voids or erosion processes (Navarro et al., 2016). This paper proposes a hydro-chemo-mechanical formulation that is capable of reproducing the free swelling behaviour of an MX-80 bentonite under different water salinity conditions. To illustrate its applicability, a set of vertical free swelling tests were simulated to demonstrate the scope and limitations of the proposed formulation.

2. Vertical free swelling tests on MX-80

2.1. Materials and methods

Wyoming MX-80 bentonite was used in the vertical free swelling tests. Its properties are similar to the material called Be-Wy–BT007-1-Sa-R that was used by Kiviranta and Kumpulainen (2011). Table 1 shows the main mineralogical, chemical, and physical properties of this natural sodium bentonite.

This material was used to produce cylindrical samples 40 mm in height and 50 mm in diameter. The initial bulk density and water content of the samples were 2.05 g/cm^3 and 17%, respectively. Deionised (DI) water was used to increase the original bentonite water content up to this value. The compacted blocks were placed at the bottom of a transparent test cell that was 50 mm in diameter (Fig. 1). Water with the desired salinity was poured on top of the samples, which allowed them to swell freely in the vertical direction. The water solutions used in the tests included DI water (one test), a 10 g/L solution (two tests), a 35 g/L solution (two tests) and a 70 g/L (one test). These solutions contained only two cations (sodium and calcium) and a common anion (chloride); their characteristics are shown in Table 2. The 10 g/L solution was a brackish-saline groundwater simulant for Olkiluoto, which is the site of the Onkalo deep geological repository for spent nuclear fuel in Finland, at the repository depth during the operational phase (based on Hellä et al., 2014). The 35 g/L solution represents the maximum expected salinity of the groundwater at the repository depth (Hellä et al., 2014) and corresponds to saline

Table 1
Properties of the tested material (Kiviranta and Kumpulainen, 2011).

Chemical composition (weight %)	
SiO_2	59.82
Al_2O_3	21.27
Fe_2O_3	3.62
Na_2O	2.86
MgO	2.77
CaO	1.49
K_2O	0.55
FeO	0.49
TiO_2	0.15
Mineralogical composition (weight %). Phases present only as traces are not shown	
Smectite	87.6
Plagioclase	4.2
Quartz	4.1
K-feldspar	1.8
Rutile	0.9
Calcite	0.6
Pyrite	0.6
Illite	0.1
Other properties	
CEC (eq/kg)	0.84
$Na^+/K^+/Ca^{2+}/Mg^{2+}$ (eq/kg)	0.58/0.02/0.25/0.08
Bentonite density $\rho_{mineral}$ (g/cm^3)	2.78
Liquid limit	510
Plastic limit	50
Plasticity index	470

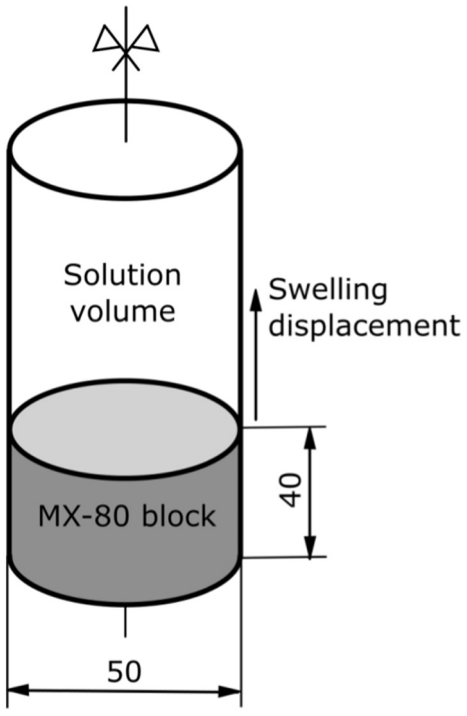

Fig. 1. Setup of the vertical free swelling test (initial dimensions in mm).

Table 2
Compositions of the permeant solutions used in the tests.

Solution	TDS (g/L)	NaCl (g/L)	$CaCl_2$ (g/L)	Number of tests
Brackish-saline water	10	6.47	3.53	2
Saline water	35	16.75	18.25	2
Highly saline water	70	26.58	43.42	1

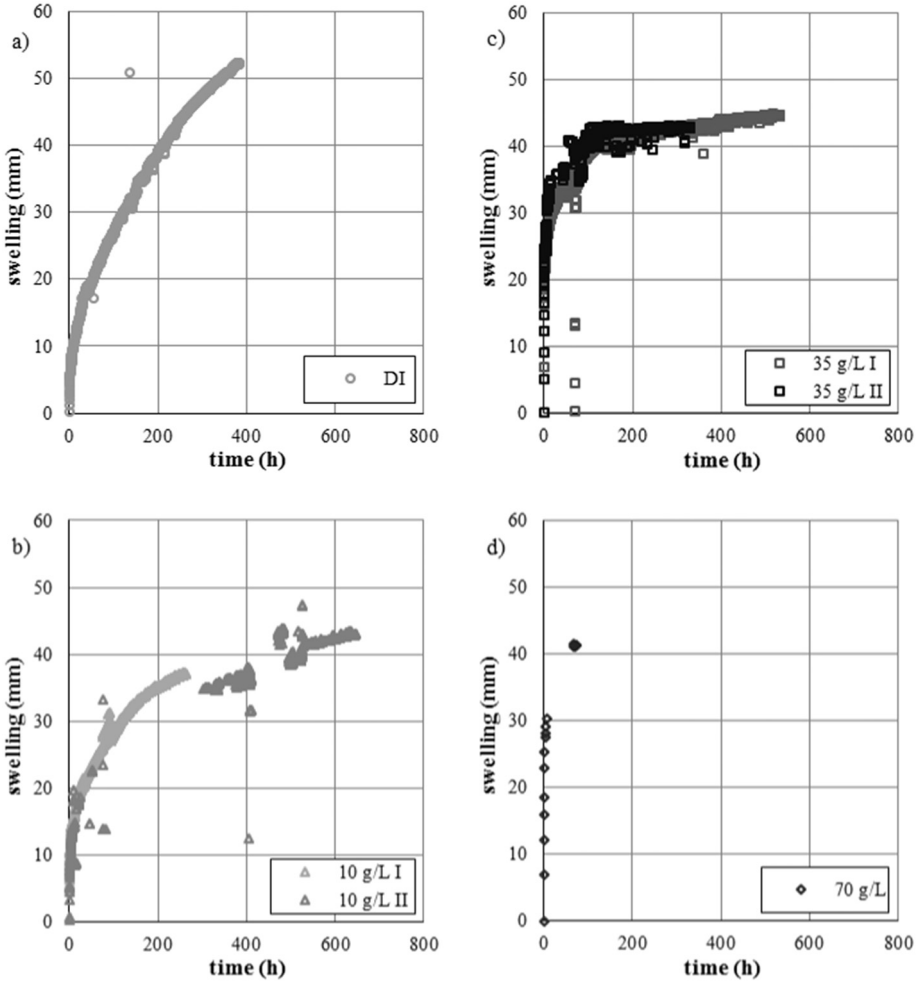

Fig. 2. Results of the vertical free swelling tests: vertical displacement of the top of the samples versus time for (a) DI water and solutions with salt contents of (b) 10 g/L, (c) 35 g/L and (d) 70 g/L.

water with a Ca^{2+}/Na^{+} mass ratio of 1:1. The 70 g/L solution represents the maximum allowable salinity of the groundwater in the vicinity of the repository (Hellä et al., 2014) and corresponds to highly saline water with a Ca^{2+}/Na^{+} mass ratio of 3:2.

During the tests, the bentonite samples were monitored using a National Instruments automated camera, and the vertical displacements of the top of the samples were computed from the images obtained using a previously calibrated digital image correlation technique in the NI Vision Builder for Automated Inspection software.

2.2. Results and analyses

Fig. 2 shows the results. A comparison of the first three graphs confirms that the rate of the swelling process increases as the salinity increases, as was noted by Alawaji (1999). The increase of the rate appears to stabilise when the salinity is high because no significant differences in the swelling rates are observed between the 35 and 70 g/L tests. Furthermore, consistent with the reduction of the swelling pressure that was observed by Karnland et al. (2005), the swelling strain at the end of the tests decreases with increasing salinity.

3. Theory

3.1. Chemo-mechanical model

The bimodal distribution of the pore size that was discussed in the Introduction suggests the use of a double porosity conceptual framework to model the compacted bentonite considered in this paper. Among existing double porosity models, the versatility and scope of the Barcelona Expansive Model (BExM; Alonso et al., 1999; Gens and Alonso, 1992) has led it to become the reference model to analyse the deformational behaviour of active clays. Consequently, as in Navarro et al. (2016), the BExM was adopted as the base stress-strain constitutive model in this study. Therefore, the macrostructural strains were calculated with the Barcelona Basic Model (BBM; Alonso et al., 1990). The parameters defined in Table 3 were used. However, as a practical

Table 3
Macrostructural mechanical parameters used in the model (from Navarro et al., 2016).

Parameter	Definition	Value
k	Increase in cohesion with suction	0.1
κ_{iO}	Saturated elastic stiffness for changes in p	0.1
α_i (kPa^{-1})	Parameter of the elastic stiffness for changes in p	0
κ_{So}	Parameter of the elastic stiffness for changes in s_M	0.05
α_{Sp}	Parameter of the elastic stiffness for changes in s_M	0
α_{SS} (kPa^{-1})	Parameter of the elastic stiffness for changes in s_M	0
p_{REF} (kPa)	Parameter of the elastic stiffness for changes in s_M	10
ν	Poisson's ratio	0.35
p_C (kPa)	Reference stress of the net mean yield stress	10
λ (0)	Slope of the virgin compression curve for saturated conditions	0.15
r	Parameter of the macrostructural soil compressibility	0.8
β (kPa^{-1})	Parameter of the macrostructural soil compressibility	$2.0 \cdot 10^{-5}$
p_O^* (kPa)	Saturated pre-consolidation stress	1800
M	Slope of the critical state line	1.07

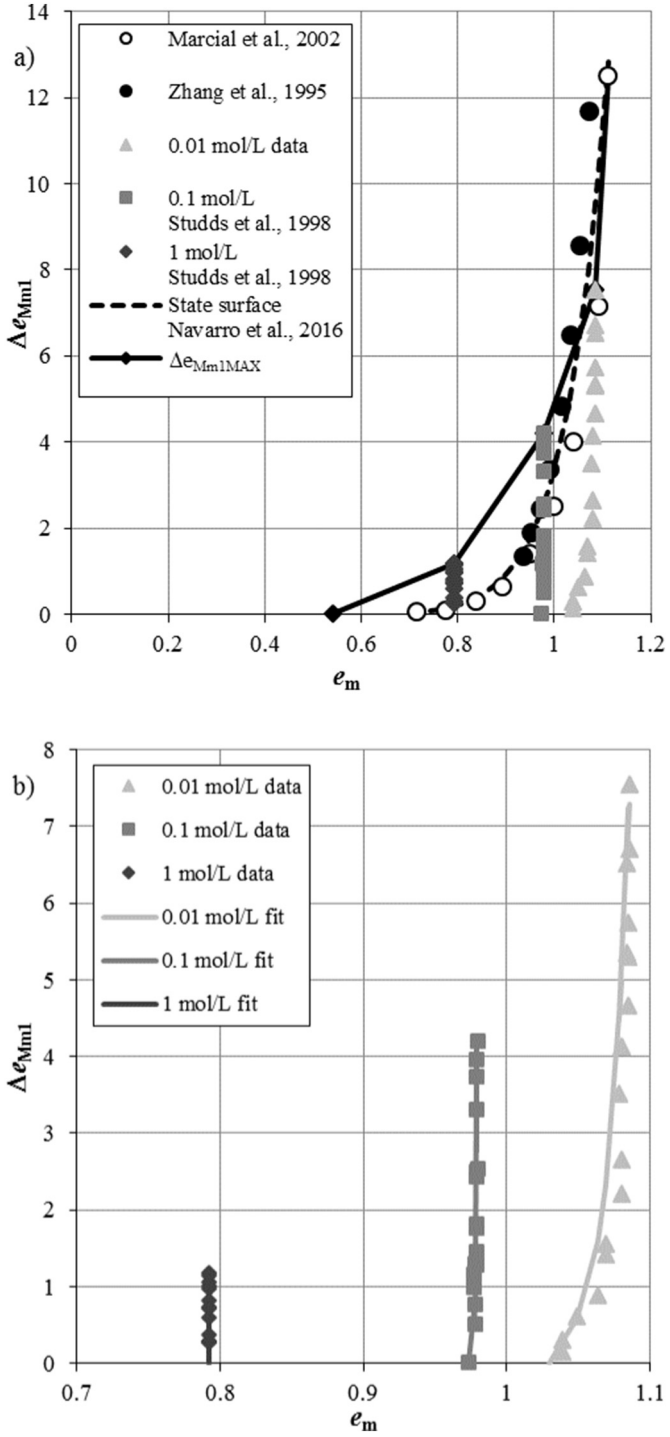

Fig. 3. (a) Increase in macroporosity not caused by stress changes in the tests by Marcial et al. (2002), Zhang et al. (1995) and Studds et al. (1998), Δe_{Mm1}. State surface proposed by Navarro et al. (2016) (dashed line), and maximum values Δe_{Mm1MAX} of Δe_{Mm1} (bold line). (b) Fits of the results from Studds et al. (1998) using Eq. (1).

approximation in the monotonic swelling paths analysed in this paper, the BBM was changed to a non-linear elastic model for total void ratio e values greater than 3. A linear relationship was assumed between log$p$ (net mean stress) and loge_M (macrostructural void ratio), adapting the formulation for deformable soils proposed by Butterfield (1979). In a manner analogous to Guimarães et al. (2013), the proportionality constant for this new linear relationship was defined such that there would be continuity for the slopes at $e = 3$.

Another relevant modification was introduced with regard to the usual application of the BExM. The model does not explicitly incorporate the macrostructural strain that is induced by bentonite destructuration and is not directly caused by mechanical loads or suction changes. In this paper, the state surface used by Navarro et al. (2016) is adapted to characterise these free swelling strains that are caused mainly by the separation of particles and aggregates that was explained in the Introduction.

Fig. 3-a shows the information from Marcial et al. (2002) and Zhang et al. (1995) that was used by Navarro et al. (2016) after analysing and adapting the experimental data obtained by these authors. The results from applying the same analysis to the test results from Studds et al. (1998) are also shown. The latter authors characterised the swelling of Wyoming bentonite saturated with distilled water when the ionic strength of the soil interstitial aqueous solution was increased to 0.01, 0.1 and 1.0 M while maintaining a constant vertical effective stress. In addition, both Marcial et al. (2002) and Zhang et al. (1995) characterised the consolidation of slurries with high initial void ratios using low salinity water. To analyse the data, the increase of the macrostructural void ratio due to free swelling, Δe_{Mm1}, for different values of the microstructural void ratio, e_m, is shown in the figure. The microstructural void ratio is defined as the volume of voids in the microstructure (intra-aggregate voids) per volume of the mineral, whereas the macrostructural void ratio, e_M, is defined as the volume of inter-aggregate voids per volume of the mineral. The rate that Δe_{Mm1} increases in the swelling tests from Studds et al. (1998) is higher than the rate with which Δe_{Mm1} decreases in the consolidation processes observed by Marcial et al. (2002) and Zhang et al. (1995). Therefore, the validity of using the state surface from Navarro et al. (2016) (dashed line in Fig. 3-a) to model the monotonic free swelling paths is questionable.

However, as noted above, the idea of using a state surface to describe Δe_{Mm1} was supported, but the new state surface, in addition to defining the dependence of Δe_{Mm1} on e_m, introduces its dependence on the salinity conditions. The paths described by Studds et al. (1998), which are contours of the state surface for constant salinity, illustrate this dependence. If the function for e_{mMAX}, which is the maximum value of the microstructural void ratio for a given salinity, is used to characterise the salinity, and the contour lines are defined through a log-log function:

$$\mathrm{Ln}\left(\frac{\Delta e_{Mm1}}{\Delta e_{Mm1\,MAX}}\right) = a \cdot \mathrm{Ln}\left(\frac{e_m}{e_{mMAX}}\right) \quad (1)$$

the satisfactory fits illustrated in Fig. 3-b are obtained. In Eq. (1), Δe_{Mm1MAX} defines the maximum value of Δe_{Mm1}, which is determined by the bold boundary line highlighted in Fig. 3-a. The coefficient a (dimensionless) characterises the rate at which Δe_{Mm1} increases as e_m increases. The fits shown in Fig. 3-b were obtained for the contour lines that correspond to 0.01, 0.1 and 1 M using a values of 74.41, 913.9 and 3750, respectively. Therefore, a is not a constant but rather a function that increases with salinity. To approximate this variability, a simplifying working hypothesis was adopted, which assumes that a remains constant for salinities less than or equal to 0.01 M as well as for salinities greater than or equal to 1 M, while it varies linearly between 0.01 M and 1 M. Thus, a is characterised by a four-segment piecewise linear function.

The subscript "1" in Eq. (1) was incorporated to the definition of Δe_{Mm} to indicate that this equation does not describe the entire variation of the macrostructural void ratio due to bentonite destructuration in a free swelling process. The data from Marcial et al. (2002), Zhang et al. (1995) and Studds et al. (1998) do not include the "explosion" that may occur in sodium bentonites when free swelling is well advanced (Neretnieks et al., 2009). In this situation, the aggregates are nearly unstructured, and there is an abundance of isolated layers. The microporosity, composed mainly by water adsorbed to the layers, is close to its maximum value and remains nearly

constant. Therefore, this large amount of swelling is mainly associated with an increase in macroporosity. In this paper, this increase is called Δe_{Mm2} as opposed to Δe_{Mm1} in Eq. (1) which is identified as the increase linked to the destructuration of aggregates. Although the physical-chemical-based modelling of Δe_{Mm2} goes beyond the scope of this paper, this term cannot be omitted from the model if the large swellings that are observed in Fig. 2 are to be reproduced. For this reason, a simplified formulation was adopted based on the parameterised expression:

$$\Delta e_{Mm2} = \alpha_{Mm2} \cdot \Delta e_{Mm1\,MAX} \cdot f_{Mm2} \tag{2}$$

where α_{Mm2} indicates the relationship between the maximum value of Δe_{Mm2} and the maximum increase in macroporosity due to the destructuration of aggregates (Δe_{Mm1MAX}, bold line in Fig. 3-a). In the models presented in the next section, a maximum value, α_{Mm2MAX}, of 10 was tentatively adopted in the swelling boundaries. In this domain, this function was assumed to be smaller by assuming that it decreases as the ratio between $\Delta e_{Mm1MAX,DI}$ (the maximum value of Δe_{Mm1MAX} for DI water, which is equal to 12.5 in accordance with Fig. 3) and Δe_{Mm1MAX} for the existing salinity decreases:

$$\alpha_{Mm2} = \alpha_{Mm2\,MAX} \cdot \frac{\Delta e_{Mm1\,MAX}}{\Delta e_{Mm1\,MAX,DI}} \tag{3}$$

The function f_{Mm2} defines how Δe_{Mm2} varies with e_m because the destructuration associated with Δe_{Mm2} initiates only when e_m is close to e_{mMAX}. As a first approximation, a piecewise linear-quadratic law was used:

$$\begin{cases} \text{if } e_m < e_{mREF}, \quad f_{Mm2} = 0 \\ \text{otherwise}, f_{Mm2} = \left(\frac{e_m - e_{mREF}}{e_{mMAX} - e_{mREF}} \right)^2 \end{cases} \tag{4}$$

Because e_{mREF} (starting threshold value of Δe_{Mm2}) is very close to e_{mMAX} (in the models shown in the next section, $e_{mREF}/e_{mMAX} = 0.98$ was used), the shape of f_{Mm2} has a limited effect on the results of the model.

Therefore, the total increase of the macrostructural void ratio caused by bentonite destructuration, Δe_{Mm}, is calculated as follows:

$$\Delta e_{Mm} = \Delta e_{Mm1} + \Delta e_{Mm2} \tag{5}$$

where Δe_{Mm1} is calculated with Eq. (1), and Δe_{Mm2} is given by Eqs. (2), (3) and (4). To use this formulation, it is necessary to define e_m. It can be obtained with the state surface defined in Fig. 4 (bold line), which is based on the experimental data from Dueck and Nilsson (2010), Kahr et al. (1990), Sane et al. (2013) and Wadsö et al. (2004). In the vertical axis e_{mR} is the remaining microstructural void ratio under dry conditions (Navarro et al., 2015), equal to 0.093 for the MX-80 bentonite analysed.

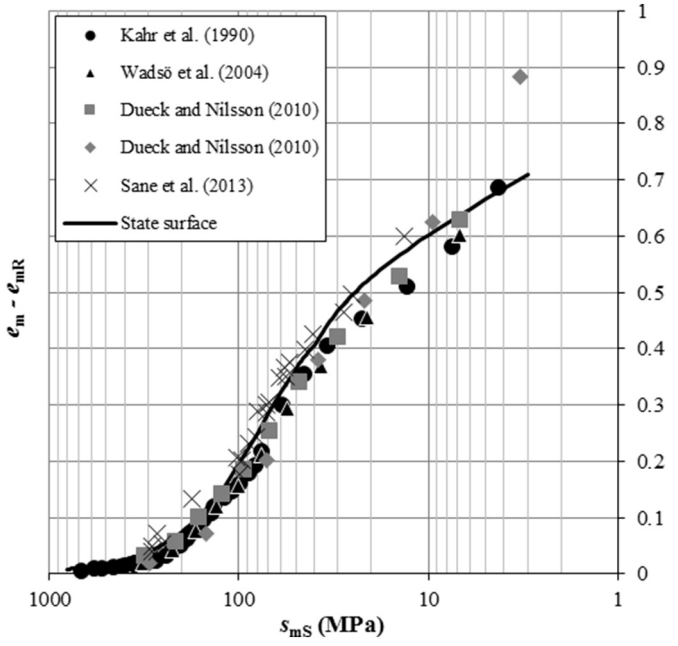

Fig. 4. State surface that defines the microstructural volumetric constitutive model.

The state surface in Fig. 4 is almost equal to that obtained using the formulation proposed by Navarro et al. (2015). However, they express e_m as a function of s_m instead of s_{mS}, and the introduction of the subscript "S" is important. Navarro et al. (2015) worked with low salinity aqueous solutions. Assuming that the concepts of total suction and water potential are equivalent (Yong, 1999), practically only matric potential was present, which is understood as the affinity of water by the solid components of the soil-water system. This affinity varies in relation to the organisation of the soil (Box and Taylor, 1962), which can be characterised by e_m for the microstructure. Consequently, Navarro et al. (2015) were able to establish a connection between e_m and s_m by identifying the total suction s_m of the microstructural water with its matric suction. However, this is not correct if the salinity is not negligible. For the same level of organisation e_m, different salinity conditions will generate different potentials.

To differentiate the microstructural matric suction from the matric suction of the macrostructure, it was called the "structural" suction with a subscript "S" in Fig. 4, s_{mS}. To calculate the increase in the microstructural suction Δs_{mO} due to "extra" salinity, namely, the contribution to the chemical potential by ions (cations and anions) in excess of the cationic exchange capacity *CEC*, the formulation introduced by Karnland et al. (2005) was adapted by introducing the microstructural osmotic coefficient φ_m:

$$\Delta s_{mO} = R \cdot T \cdot \rho_W \cdot \left(\sum_i c_{i,mNCC} \right) \cdot \phi_m \tag{6}$$

where R is the universal gas constant, T is the absolute temperature, and $c_{i,mNCC}$ is the microstructural non-charge-compensating molal concentration of the i-th ion. For simplicity, φ_m was assumed to be equal to 1 in this first approach to the problem. In addition, as noted in the Introduction, a simple geochemical model was assumed, which consists of a single type of anion, chloride Cl^-, and two types of cations, sodium Na^+ and calcium Ca^{2+}. The chloride present in the microstructure does not compensate for the negative charges of the clay particles, and it is therefore in excess. It was assumed that for sodium and calcium, there is a proportionality between the charge-compensating fraction and the total amount present in the microstructure.

Because Cl^- may be present in the microstructure, anion exclusion is not imposed (Tournassat and Appelo, 2011), but the distribution of any ion between the macro- and microstructures will be conditioned by chemical equilibrium. This equilibrium is determined by the equality of electrochemical potentials $\mu_{i,k}$ defined as:

$$\mu_{i,k} = \mu_{Oi} + R \cdot T \cdot \mathrm{Ln}\, a_{i,k} + z_i \cdot F \cdot \Psi_k \tag{7}$$

where the subscript "i" indicates the type of ion (Cl^-, Na^+, and Ca^{2+} in the model considered here), the subscript "k" can take the values "m" and "M" according to the ion present in the micro- or macrostructure, respectively, μ_{Oi} is a reference electrochemical potential, $a_{i,k}$ is the activity, z_i is the ionic charge, F is the Faraday constant, and Ψ_k is the electric potential of the ions in the micro- or macrostructure. If there is a balance between the species in the macro- and microporosities, both chemical potentials must be equal. Consequently, making $\mu_{i,m}$ equal to $\mu_{i,M}$ in Eq. (7) results in:

$$a_{i,M} = a_{i,m} \cdot \exp\left(\frac{z_i \cdot F \cdot \Psi_D}{R \cdot T} \right) \tag{8}$$

where Ψ_D is the Donnan potential, which is defined as $\Psi_D = \Psi_m - \Psi_M$. If an approximate model is adopted in which the activity coefficients are equal to 1, consistent with the osmotic coefficients, then a Donnan

electrochemical equilibrium model between the macro- and microstructures is obtained, such as that proposed by Tournassat and Appelo (2011):

$$C_{i,M} = C_{i,m}\cdot\exp\left(\frac{z_i\cdot F\cdot\Psi_D}{R\cdot T}\right) = \frac{C_{i,m}}{B^{z_i}} \quad (9)$$

where $C_{i,M}$ and $C_{i,m}$ are the molar concentrations in both structural levels, and B is the partitioning function for the ion concentrations in the macro- and microstructures, which is common for all of the ions present in the system. Additionally, electro-neutrality of the system must be met:

$$C_{Na,M} + 2\cdot C_{Ca,M} - C_{Cl,M} = 0 \quad (10)$$

$$C_{Na,m} + 2\cdot C_{Ca,m} - C_{Cl,m} - q = 0 \quad (11)$$

where q is the surface charge (mol_c/L), which can be calculated as:

$$q = \frac{CEC\cdot\rho_{mineral}}{e_m} \quad (12)$$

where $\rho_{mineral}$ is the mineral density. Table 1 shows the *CEC* and $\rho_{mineral}$ values of the analysed bentonite. If $C_{Ca,M}$ and $C_{Cl,m}$ are adopted as state variables of the electrochemical problem (their calculation is explained in the next subsection), it can be derived from Eqs. (9) to (11) that:

$$-(2C_{Ca,M} + C_{Cl,m})\cdot B^2 + 2\cdot C_{Ca,M}\cdot B + C_{Cl,m} + q = 0 \quad (13)$$

which is a quadratic functional expression that allows B (and therefore Ψ_D) to be determined. Once B is known, $C_{Ca,m}$ and $C_{Cl,M}$ are obtained from $C_{Ca,M}$ and $C_{Cl,m}$, respectively. Then, $C_{Na,M}$ and $C_{Na,m}$ are obtained using Eqs. (10) and (11) (electroneutrality).

Once the electrochemical problem has been solved, the concentrations of the chemical species in the microstructure allow Δs_{mO} to be calculated using Eq. (6). However, because s_{mS} is still unknown, the calculation of e_m is not possible. It can be assumed that e_m is also a state variable that can be calculated by analysing the mass balance of the microstructural water (e.g., Navarro et al., 2016). However, in this paper, a simpler strategy was adopted by assuming that there is equilibrium between the water from the macro- and microstructures. By accepting this hypothesis, equality of the chemical potentials is imposed, and the chemical potential of the microstructural water, μ_m, is calculated based on the potential of the macrostructural water, μ_M. Based on this and by knowing Δs_{mO}, s_{mS} can be calculated as described in the following paragraphs, which is used to obtain e_m. The hypothesis of equilibrium between the macro- and microstructural water is questionable (Ferrage et al., 2007) because it entails not characterising the kinetics of the process of mass exchange between the macro- and microstructure but rather considering it to be instantaneous. However, it is perhaps the hypothesis that is most consistent with having assumed that the dissolved species in both types of water are in equilibrium.

The chemical potential of the macrostructural water μ_M can be obtained using (Karnland et al., 2005):

$$\mu_M = \mu_{VO}(T) - \frac{WMM}{\rho_W}\cdot(s_M + s_{MO}) \quad (14)$$

where $\mu_{VO}(T)$ is the chemical potential of pure water at a temperature T, *WMM* is the molar mass of water, ρ_W is the density of free water, and s_M is the macrostructural matric suction. It is identified with the capillary suction and is thus defined as the difference between the gas pressure and the liquid pressure P_L, $s_M = P_G - P_L$. In addition, s_{MO} is the macrostructural osmotic suction that, as in Eq. (6), is defined as:

$$s_{MO} = R\cdot T\cdot\rho_W\cdot\left(\sum_i c_{i,M}\right)\cdot\phi_M \quad (15)$$

where $c_{i,M}$ is the molal concentration of the i-th ion in the macrostructural porosity, and φ_M is the macrostructural osmotic coefficient. As with the microstructural water, φ_M will be 1.

Therefore, the chemical potential of the microstructural water μ_m can be calculated as:

$$\mu_m = \mu_{mS} + \Delta\mu_{mO} \quad (16)$$

where, based on the definition of s_{mS} and as proposed by Navarro et al. (2016) and Karnland et al. (2005), the structural potential can be expressed as:

$$\mu_{mS} = \mu_{VO}(T) + \frac{WMM}{\rho_m}\cdot(p - s_{mS}) \quad (17)$$

where ρ_m is the microstructural water density, and p is the net mean stress (defined as the mean stress minus the gas pressure). Additionally, the increase in chemical potential associated with Δs_{mO} that is caused by the "extra" salinity is given by:

$$\Delta\mu_{mO} = -\frac{WMM}{\rho_m}\cdot\Delta s_{mO}. \quad (18)$$

Several studies have shown that the density of adsorbed water is greater than that of free water (e.g. Jacinto et al., 2012). However, as proposed in Tournassat and Appelo (2011), $\rho_m = \rho_W$ was assumed for modelling purposes. Therefore, if $\mu_M = \mu_m$ is used, it is derived from Eqs. (14) to (18) that:

$$s_{mS} = p + s_M + s_{MO} - \Delta s_{mO} \quad (19)$$

which allows the state surface of Fig. 4 to be applied to determine e_m.

To finish this subsection, the method used to calculate the value of e_{mMAX} used in Eqs. (1) and (4) should be defined. According to Fig. 4, the maximum microstructural void ratio possible for a given salinity occurs when the structural suction of the microstructure is minimal, s_{mSmin}. In accordance with Eq. (19), this occurs when $p = 0$ (unconfined conditions) and $s_M = 0$ (saturated conditions), which satisfy $s_{mSmin} = s_{MO} - \Delta s_{mO}$. By introducing this value in Fig. 4, e_{mMAX} is obtained.

3.2. Flow and transport model

Isothermal problems that assume a constant gas pressure value equal to atmospheric pressure were analysed. Therefore, the flow problem concentrated on the analysis of liquid water and vapour. Both flows occur only in the macrostructure. As usual (e.g., Yong, 1999), the microstructure was assumed to be saturated, and therefore, there is no point in considering the vapour flow in it. Additionally, as in van Genuchten and Wierenga (1976), the microstructural water was assumed to be primarily linked to the bentonite, and thus, the microstructural flow vector $\mathbf{v}_m$ was assumed to equal $\mathbf{v}$ (the time derivative of the soil skeleton's displacements $\mathbf{u}$, which is obtained by solving the mechanical problem associated with the mechanical equilibrium equation). The conventional advective (Darcy) formulation proposed by Pollock (1986) was used to model the macrostructural water flow. Osmotic problems, such as those evaluated by Malusis et al. (2003), were not taken into account. The electro-osmotic flows associated with the Donnan potential gradients were also not considered. Therefore, using the parameters in Table 4, a flow model similar to that described in detail by Navarro et al. (2016) was used, although the flow of water vapour in the macrostructure was not neglected. Assuming a constant gas pressure, the mass flow of vapour is only diffusive, and it can therefore be calculated by Fick's law using the

Table 4
Hydraulic parameters of the macrostructure.

Parameter	Definition	Value
α (kPa^{-1})	van Genuchten (1980) parameter	1.15×10^{-4}
m	van Genuchten (1980) parameter	0.733
b_M	Intrinsic permeability parameter	9.911
ϕ_{M0}	Intrinsic permeability parameter	0.047
k_0 (m^2)	Intrinsic permeability parameter	2.339×10^{-21}

approach proposed by Pollock (1986) assuming a soil tortuosity equal to 1.

The microstructural water mass balance equation allows the mass exchange, $r_{m.}$, between the macro- and microstructures to be determined based on the value of e_m obtained using the calculations in the previous subsection. Consequently, P_L (obtained after solving the macrostructural water mass balance equation) is the only state variable for the flow.

The previous subsection also described that the concentrations $C_{Ca,M}$ and $C_{Cl,m}$ were selected as state variables of the transport. To determine these concentrations, the total mass balance of the species dissolved in water was analysed:

$$\frac{\partial m_i}{\partial t} + \nabla\cdot(m_i\cdot\mathbf{v}_i) = 0 \tag{20}$$

where the mass of the i-th ion per unit volume m_i is given by:

$$m_i = m_{i,M} + m_{i,m} = \frac{C_{i,M}\cdot Sr_M\cdot e_M + C_{i,m}\cdot e_m}{1+e} \tag{21}$$

where $m_{i,M}$ defines the mass of the solute per unit volume in the macrostructure, $m_{i,m}$ has an analogous definition in the microstructure, Sr_M is the macrostructural degree of saturation, e_M defines the macrostructural void ratio, and e is the total void ratio (total volume of voids per volume of mineral, $e = e_m + e_M$). Although i = Ca^{2+} or Cl^- in the analyses performed in this paper, the proposed framework is valid for any other species.

The term $m_i\cdot\mathbf{v}_i$ in Eq. (20) defines the mass flow of solute per unit area, which is calculated as:

$$m_i\cdot\mathbf{v}_i = m_i\cdot\mathbf{v} + \mathbf{l}_i \tag{22}$$

where the mass flow of the i-th ion with regard to the soil skeleton's displacement, $\mathbf{l}_i$, is given by:

$$\mathbf{l}_i = m_{i,M}\cdot\mathbf{q}_M + \mathbf{j}_{i,M} + \mathbf{j}_{i,m}. \tag{23}$$

The term $m_{i,M}\cdot\mathbf{q}_M$ defines the advective flow in the macrostructure because the vector $\mathbf{q}_M$ identifies the macrostructural water seepage. Like the microstructural water, the advective term was assumed to be null in the microstructure. The vectors $\mathbf{j}_{i,M}$ and $\mathbf{j}_{i,m}$ are the diffusion of the i-th ion in the macrostructure with respect to the advective flow and the diffusion of the i-th ion in the microstructural liquid, respectively. The macro diffusion was modelled using Fick's law:

$$\mathbf{j}_{i,M} = -\frac{e_M\cdot Sr_M}{1+e} D_{i,M}\nabla C_{i,M} \tag{24}$$

where $D_{i,M}$ is the macrostructural molecular diffusion coefficient (diffusion is considered isotropic). Because the modulus of the advective flow is usually small, mechanical dispersion was neglected. The formulation by Bourg et al. (2006) was adopted to determine $D_{i,M}$:

$$D_{i,M} = D_{o,i}\frac{1}{G} \tag{25}$$

where $D_{o,i}$ is the self-diffusion coefficient of the i-th ion in bulk liquid water, and G is a factor that accounts for the influence of the pore-network geometry and was assumed to be 4. The values used for the self-diffusion coefficients are $D_{o,Ca2+} = 7.79\cdot10^{-10}$ m^2/s and $D_{o,Cl-} = 2.03\cdot10^{-9}$ m^2/s (Cussler, 1997). In the present formulation, the micro diffusion was neglected due to lack of data on the microstructural diffusion coefficient, $\mathbf{j}_{i,m} = \mathbf{0}$.

3.3. Numerical implementation

The proposed hydro-mechanical-electrochemical model was implemented in COMSOL Multiphysics (CM), which is a multiphysics partial differential equation solver that is based on the application of the finite element method with Lagrange multipliers (COMSOL, 2015). This finite element model is based on a hydro-mechanical numerical model that was developed by the research group of the authors of this paper. The strategies and numerical skills described in Navarro et al. (2014, 2016) were applied.

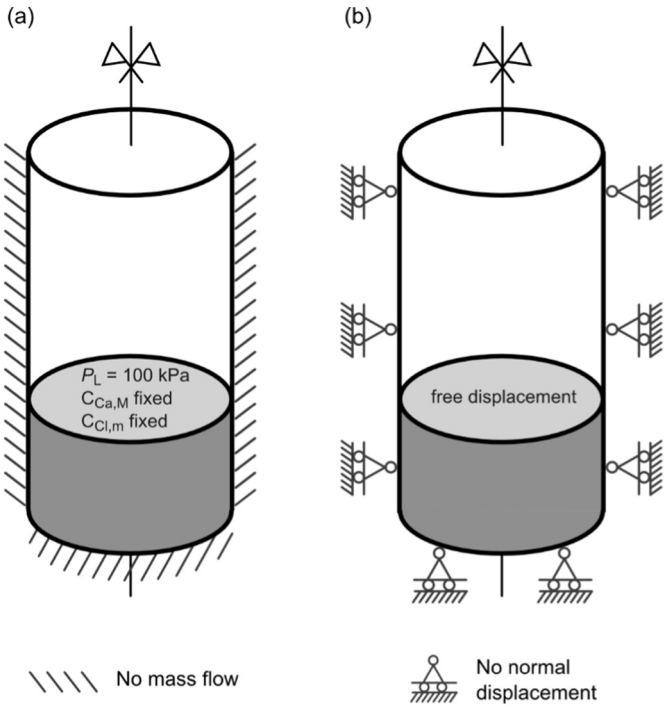

Fig. 5. Boundary conditions used in the simulations: (a) for the flow and transport problem, in which the ion concentrations fixed at the top correspond to those of the corresponding permeant solution, and (b) for the mechanical problem.

4. Results and discussion

To analyse the scope of the proposed formulation, the vertical free swelling tests described in Section 2 were analysed using a 2D axisymmetric model. The initial and boundary conditions shown in Fig. 5 were applied. In the mass balance of the chemical species, the ion concentrations fixed at the top were those of the permeant solution that corresponded to each test (Table 2).

First, the tests were simulated without considering the salinity effect. This model, named model M1, assumed that distilled water (DI) was used. Obviously, by not considering the salinity, there is only one result, which is compared with the results obtained experimentally for each salinity in Figs. 6-a to -d. As expected, the fit for the DI case is good, but the fits for the other solutions are inadequate.

To improve the behaviour of model M1 for brackish and saline waters, the full electro-chemo-hydro-mechanical formulation presented above was used to model the tests. However, in the Δe_{Mm} model (i.e., Eqs. (1) to (5)), the parameters for DI water were used: $\Delta e_{Mm1MAX,DI} = 12.5$, $e_{mMAX,DI} = 1.1$, and $a = 74.4$. This model was called model M2, and the swelling results obtained from it are plotted in Figs. 6-e to -h. The increased presence of ions in the non-negligible salinity cases, which results from the infiltration of a more saline external water, increases the chemical potential of the macrostructural water and thus the microstructural water as well. Both the osmotic and structural suctions increase. In other words, the microstructure becomes more ordered, and the microstructural void ratio decreases (Fig. 7). This effect has been called “osmotic shrinkage” by some authors (e.g., Lloret and Villar, 2007) and causes the swelling capacity to decrease as the water salinity increases, as in the experimental results (Section 2). However, M2 does not reproduce the other effect caused by the salinity, which is the increase in the swelling rate. For the times analysed, the predictions of M2 are significantly lower than the experimental results (Figs. 6-f to -h).

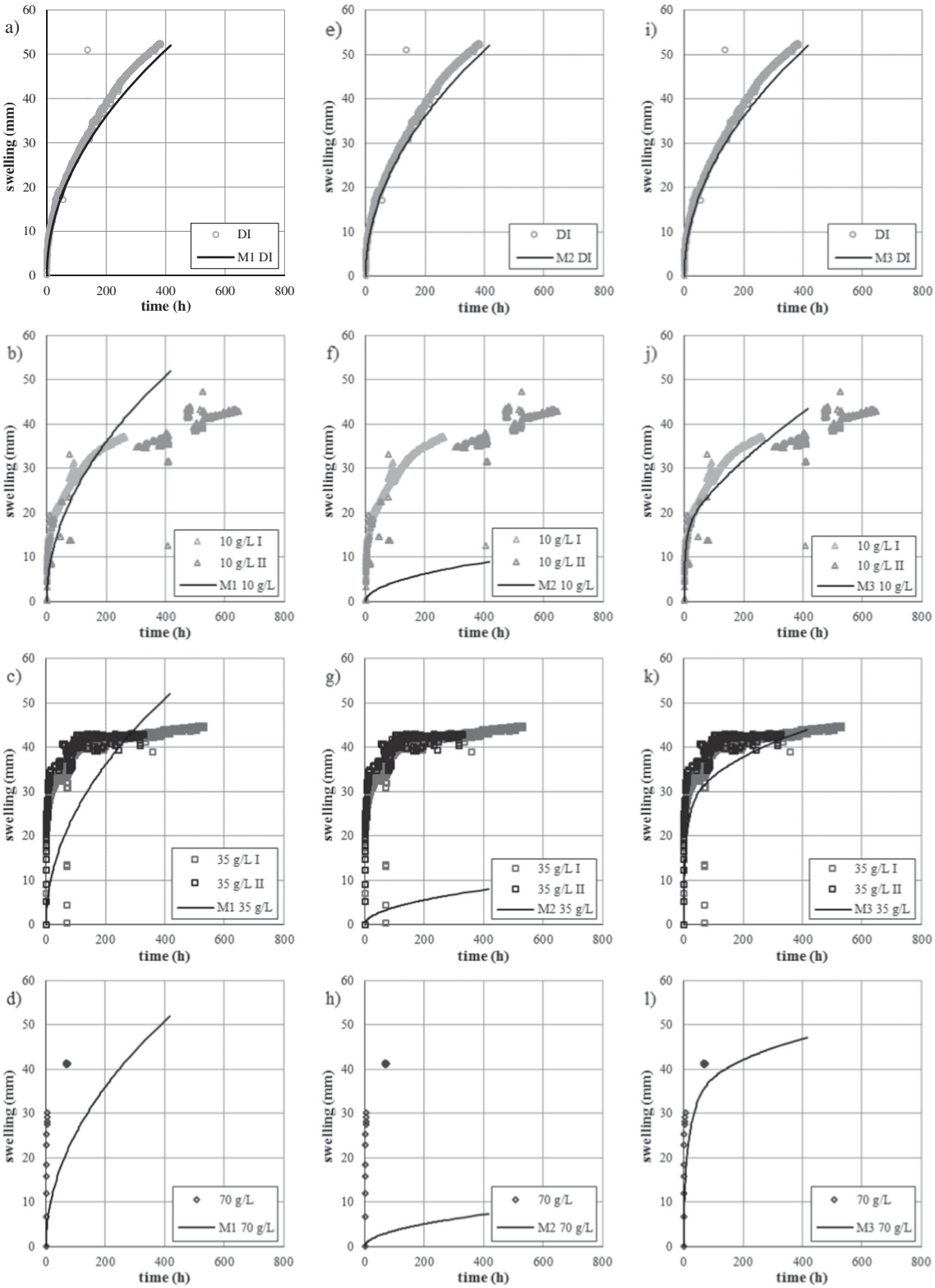

Fig. 6. Vertical free swelling tests (Table 2) and model results. Model M1: (a) DI water, (b) 10 g/L, (c) 35 g/L and (d) 70 g/L salt contents. Model M2: (e) DI, (f) 10 g/L, (g) 35 g/L and (h) 70 g/L salt contents. Model M3: (i) DI, (j) 10 g/L, (k) 35 g/L and (l) 70 g/L salt contents.

In the free swelling paths, both the total and macrostructural void ratios increase. These increases are significantly greater than the increase of e_M caused by the reduction of e_m under confined conditions due to the salinity. For this reason, in the free swelling paths, the osmotic shrinkage alone does not explain the increase in the swelling rate. It is advisable to adopt a formulation in which the macrostructure growth rate increases with salinity, while the total swelling decreases. In other words, the behaviour of the results by Studds et al. (1998) that are shown in Fig. 3 must be reproduced, which is achieved when the formulation of Δe_{Mm} defined by Eqs. (1)–(5) is "correctly" applied. If (i) Δe_{Mm1MAX} is determined from the bold line in Fig. 3, (ii) e_{mMAX} is calculated as described in the last paragraph of Subsection 3.1, and (iii)

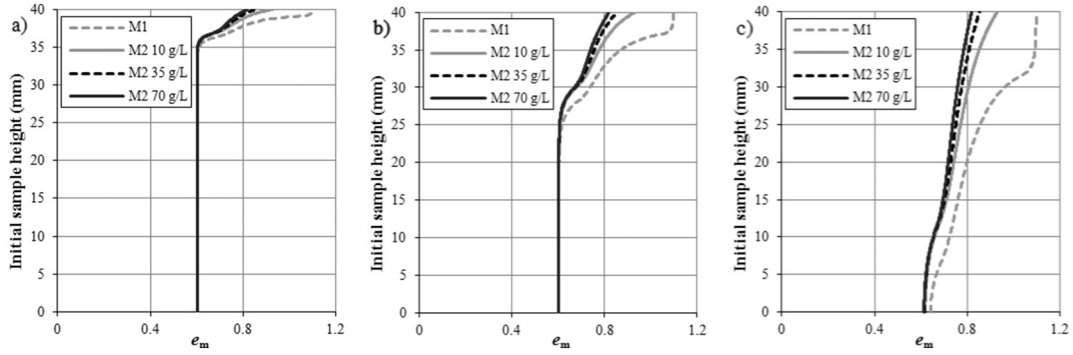

Fig. 7. Comparisons of the microstructural void ratios e_m obtained with models M1 and M2. Time: (a) 5 h, (b) 50 h, and (c) 400 h.

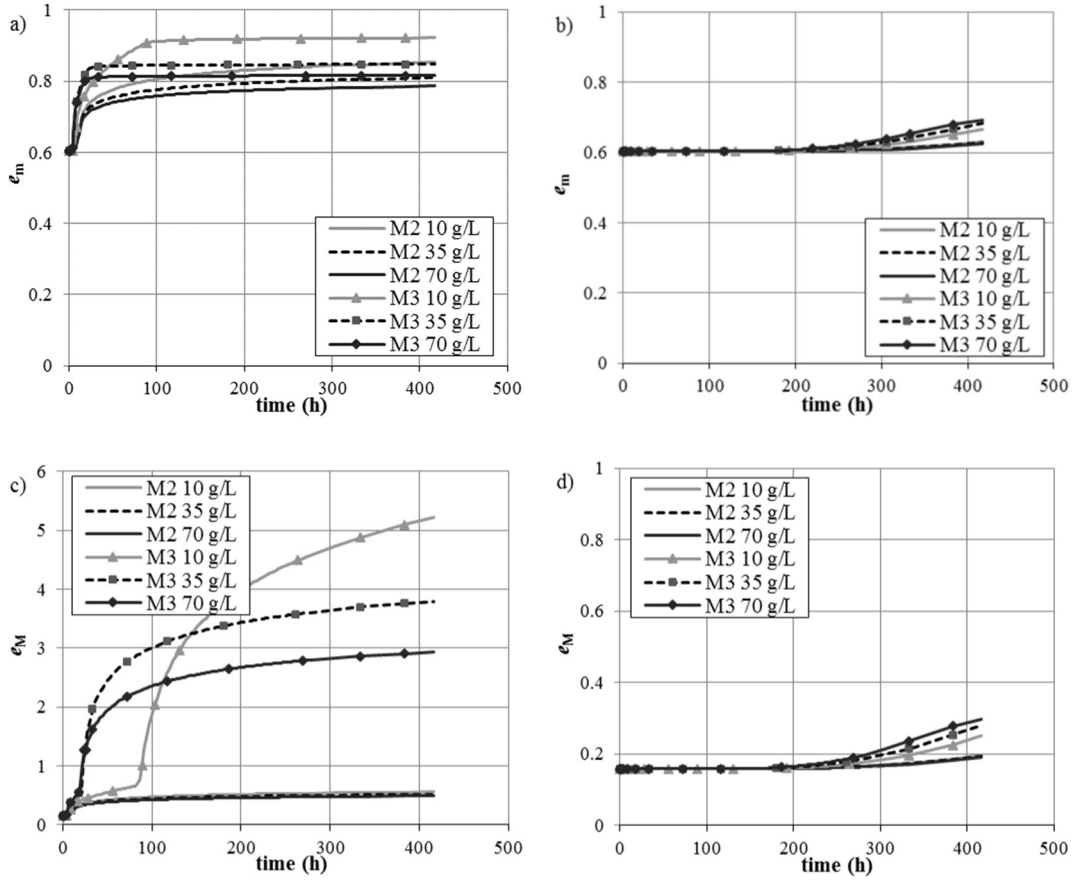

Fig. 8. Comparisons of the results of models M2 and M3 at points P1 and P2. Microstructural void ratios of (a) P1 and (b) P2. Macrostructural void ratios of (c) P1 and (d) P2.

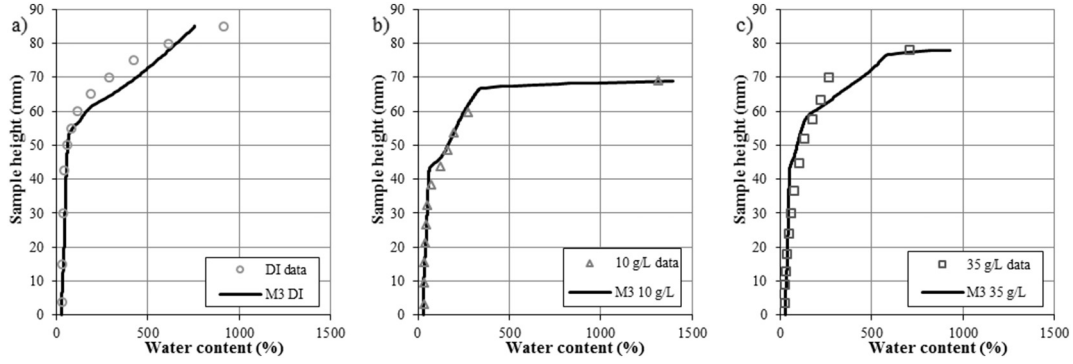

Fig. 9. Water content distributions at the end of the tests. Dots are experimental data, and lines are model predictions (M3) for: (a) DI, (b) 10 g/L and (c) 35 g/L.

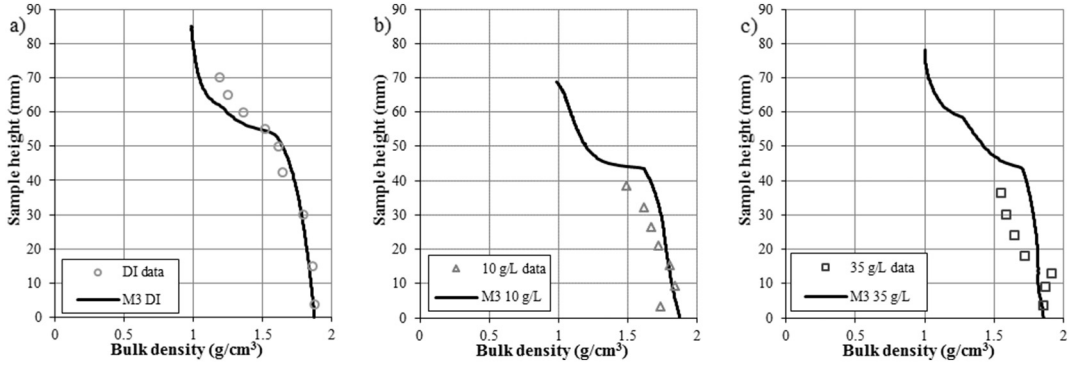

Fig. 10. Bulk density distributions at the end of the tests. Dots are experimental data, and lines are model predictions (M3) for (a) DI, (b) 10 g/L and (c) 35 g/L.

the value of a to use in Eq. (1) is computed using the piecewise function defined in Subsection 3.1, the results identified as M3 in Figs. 6-i to 6-l are obtained. These results significantly improve upon those of model M2. This is also observed in Fig. 8, which compares the predicted evolutions of e_m and e_M at two points on the sample that are initially located 0.5 cm from the top, P1, and from the bottom, P2. The hydration barely affects P2. As shown in Fig. 9, the water conditions hardly varied in the lower half of the sample. Consequently, the void ratios obtained with M2 and M3 are comparable. However, the situation is different at P1. The evolution of e_m is not significantly different because the effect of the salinity on e_m is included in both M2 and M3. Nevertheless, the salinity also changes e_{mMAX} and consequently the point at which Δe_{Mm} is activated, which causes e_M to increase earlier and thus modifies the swelling behaviour. Because this salinity effect is only included in model M3, there are significant differences between the predictions of M2 and M3, as shown in Fig. 3.

Regardless of how the effect of salinity on Δe_{Mm} is simulated, the same result is always obtained for DI water. For this reason, Figs. 6-a, -e and -i are the same, and the latter two figures could therefore probably be ignored. However, the comparison is illustrated more clearly with their inclusion.

The proposed model (M3) captures the trend of the swelling and, as shown in Figs. 9 and 10, the distributions of the water content and bulk density in the bentonite (no experimental data of these variables were obtained from the 70 g/L test). It is important to emphasise that very high water contents were obtained in the tests with e values of 40. As shown in Figs. 10-a to -c, the bulk density decreased so much that it could not be measured reliably at the top of the test piece, which calls into question the validity of the assumption that the material remains a "soil" in the context of Soil Mechanics. The fits reveal that the formulation proposed by Eqs. (1)–(5) has the ability to simulate large swellings. However, it is still not possible to accurately reproduce the high swelling rate observed experimentally at the beginning of the tests.

To conclude this section, Fig. 11 shows the evolution of the ratio of calcium cations Ca^{2+} to the total charge-compensating cations, X_{Ca2+}, which is defined as $X_{Ca2+} = C_{Ca,mCC} / (C_{Ca,mCC} + C_{Na,mCC})$. The results are associated with the complete model, M3. This magnitude is of great relevance given the influence of the charge-compensating cations on swelling (Zhu et al., 2015). However, X_{Ca2+} remained less than 80% throughout all of the tests. Consequently, according to Birgersson et al. (2009), the behaviour of the bentonite was always that of a sodium bentonite. This is consistent with the high swelling value that was obtained. In addition, this supports the use of the same deformational model in all of the simulations without considering the variation in the distribution of the charge-compensating cations.

5. Conclusions

Despite its limitations, the proposed formulation allows for the consistent inclusion of the effect of water salinity on the swelling of MX-80 bentonite. The inclusion of the osmotic terms into both the micro- and macrostructural levels in the chemo-hydro-mechanical formulation models the limiting effect of salinity on the swelling capacity that was observed experimentally in vertical free swelling tests using solutions with salt contents between 10 and 70 g/L of sodium and calcium chloride. In addition, the formulation proposed in Eqs. (1)–(5) reproduces the increase of the destructuration rate of bentonite and, as a result, the swelling rate caused by the salinity. These additions to the model significantly improve the predictions compared to those that do not account for the salinity effects. Although the fit could be improved further for the swelling velocity in the shorter term (likely by improving the flow and transport model as well as the increase of the macrostructural void ratio that occurs when the aggregates are nearly destructured), the proposed formulation is a useful starting point to characterise the effect of salinity on the free swelling of compacted bentonites.

Acknowledgements

This study was funded in part by B + Tech Oy (Finland) under a

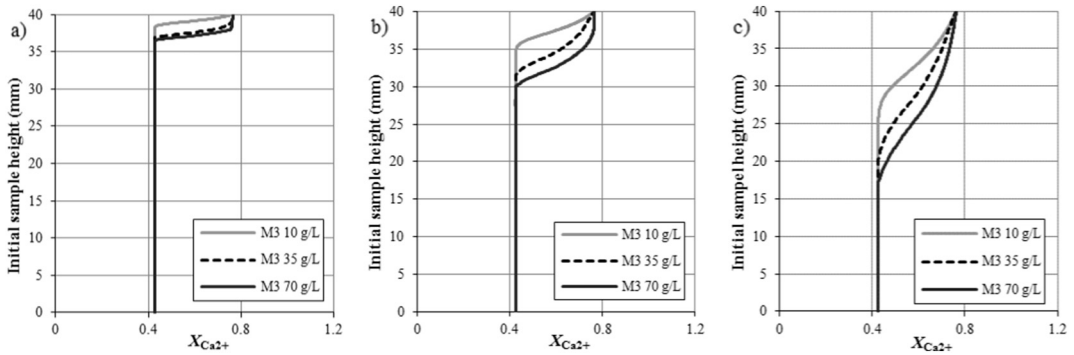

Fig. 11. Evolution of the ratio of Ca^{2+} cations to the total charge-compensating cations, X_{Ca2+}, for model M3. Time: (a) 5 h, (b) 50 h, and (c) 400 h.

Posiva Oy project and by FPU Grant FPU15/02655 from the Spanish Ministry of Education, Culture and Sport, which was awarded to Ms. De la Morena. The contributions of Dr. Petri Sane and Ms. Noora Kanerva to the completion of the laboratory tests are greatly appreciated. The authors express their gratitude to Dr. Kari Koskinen for managing and following up on the project.

References

Alawaji, H.A., 1999. Swell and compressibility characteristics of sand-bentonite mixtures inundated with liquids. Appl. Clay Sci. 15 (3–4), 411–430. http://dx.doi.org/10.1016/S0169-1317(99)00033-2.

Alonso, E.E., Gens, A., Josa, A., 1990. A constitutive model for partially saturated soils. Géotechnique 40 (3), 405–430.

Alonso, E.E., Vaunat, J., Gens, A., 1999. Modelling the mechanical behaviour of expansive clays. Eng. Geol. 54 (1–2), 173–183. http://dx.doi.org/10.1016/S0013-7952(99)00079-4.

Birgersson, M., Börgesson, L., Hedström, M., Karnland, O., Nilsson, U., 2009. Bentonite Erosion. Final Report. SKB Technical Report TR-09-34. Svensk Kärnbränslehantering AB. Swedish Nuclear Fuel and Waste Management Co. See:. www.skb.com/publication/1975568/TR-09-34.pdf last accessed March 2017.

Bourg, I.C., Sposito, G., Bourg, A.C.M., 2006. Tracer diffusion in compacted, water-saturated bentonite. Clay Clay Miner. 54 (3), 363–374.

Box, J.E., Taylor, S.A., 1962. Influence of soil bulk density on matric potential. Soil Sci. Soc. Am. J. 26 (2), 119–122. http://dx.doi.org/10.2136/sssaj1962.03615995002600020008x.

Burton, G.J., Pineda, J.A., Sheng, D., Airey, A., 2015. Microstructural changes of an undisturbed, reconstituted and compacted high plasticity clay subjected to wetting and drying. Eng. Geol. 193, 363–373. http://dx.doi.org/10.1016/j.enggeo.2015.05.010.

Butterfield, R., 1979. A natural compression law for soils (an advance on e-log p'). Géotechnique 29 (4), 469–480.

Cases, J.M., Bérend, I., Besson, G., François, M., Uriot, J.P., Thomas, F., Poirier, J.E., 1992. Mechanism of adsorption and desorption of water vapor by homoionic montmorillonite. 1. The sodium-exchanged form. Langmuir 8 (11), 2730–2739.

COMSOL, 2015. COMSOL Multiphysics Reference Manual, version 5.1 .

Cussler, E.L., 1997. Diffusion: Mass Transfer in Fluid Systems, second ed. Cambridge University Press.

Dueck, A., Nilsson, U., 2010. Thermo-Hydro-Mechanical properties of MX-80. Results from advanced laboratory tests. SKB Technical Report TR-10-55. Svensk Kärnbränslehantering AB. Swedish Nuclear Fuel and Waste Management Co. See:. www.skb.com/publication/2223073/TR-10-55.pdf last accessed March 2017.

Ferrage, E., Kirk, C.A., Cressey, G., Cuadros, J., 2007. Dehydration of Ca-montmorillonite at the crystal scale. Part 2. Mechanisms and kinetics. Am. Fortschr. Mineral. 92 (7), 1007–1017. http://dx.doi.org/10.2138/am.2007.2397.

Gens, A., Alonso, E.E., 1992. A framework for the behaviour of unsaturated expansive clays. Can. Geotech. J. 29 (6), 1013–1032.

van Genuchten, M.T., 1980. A closed-form equation for predicting the hydraulic conductivity of unsaturated soils. Soil Sci. Soc. Am. J. 44 (5), 892–898.

van Genuchten, M.T., Wierenga, P.J., 1976. Mass transfer studies in sorbing porous media I. Analytical solutions. Soil Sci. Soc. Am. J. 40 (4), 473–480.

Guimarães, L.D.N., Gens, A., Sánchez, M., Olivella, S., 2013. A chemo-mechanical constitutive model accounting for cation exchange in expansive clays. Géotechnique 63 (3), 221–234. http://dx.doi.org/10.1680/geot.SIP13.P.012.

Hellä, P., Pitkänen, P., Löfman, J., Partamies, S., Vuorinen, U., Wersin, P., 2014. Safety Case for the Disposal of Spent Nuclear Fuel at Olkiluoto - Definition of Reference and Bounding Groundwaters, Buffer and Backfill Porewaters. Posiva Report 2014-04. Posiva Oy See:. www.posiva.fi/files/3634/POSIVA_2014-04.pdf last accessed March 2017.

Jacinto, A.C., Villar, M.V., Ledesma, A., 2012. Influence of water density on the water-retention curve of expansive clays. Géotechnique 62 (8), 657–667. http://dx.doi.org/10.1680/geot.7.00127.

Kahr, G., Kraehenbuehl, F., Stoeckli, H.F., Muller-von Moos, M., 1990. Study of the water-bentonite system by vapour adsorption, immersion calorimetry and X-ray techniques. II. Heats of immersion, swelling pressures and thermodynamic properties. Clay Miner. 25 (4), 499–506.

Karnland, O., Muurinen, A., Karlsson, F., 2005. Bentonite swelling pressure in NaCl solutions. Experimentally determined data and model calculations. In: Alonso, E.E., Ledesma, A. (Eds.), Advances in Understanding Engineered Clay Barriers: Proceedings of the International Symposium on Large Scale Field Tests in Granite, Sitges, Barcelona, 12–14 November 2003. Taylor and Francis Group, London, pp. 241–256.

Kiviranta, L., Kumpulainen, S., 2011. Quality control and characterization of bentonite materials. Posiva Working Report 2011-84. Posiva Oy See:. www.posiva.fi/files/1994/WR_2011-84_web.pdf last accessed March 2017.

Lloret, A., Villar, M.V., 2007. Advances on the knowledge of the thermo-hydro-mechanical behaviour of heavily compacted "FEBEX" bentonite. Phys. Chem. Earth 32 (8–14), 701–715. http://dx.doi.org/10.1016/j.pce.2006.03.002.

Malusis, M.A., Shackelford, C.D., Olsen, H.W., 2003. Flow and transport through clay membrane barriers. Eng. Geol. 70, 235–248. http://dx.doi.org/10.1016/S0013-7952(03)00092-9.

Marcial, D., Delage, P., Cui, Y.J., 2002. On the high stress compression of bentonites. Can. Geotech. J. 39 (4), 812–820. http://dx.doi.org/10.1139/t02-019.

Marry, V., Rotenberg, B., 2015. Chapter 11 - Upscaling strategies for modeling clay-rock properties. In: Tournassat, C., Steefel, C.I., Bourg, I.C., Bergaya, F. (Eds.), Developments in Clay Science. Elsevier, pp. 399–417.

Mašín, D., 2013. Double structure hydromechanical coupling formalism and a model for unsaturated expansive clays. Eng. Geol. 165, 73–88. http://dx.doi.org/10.1016/j.enggeo.2013.05.026.

Navarro, V., Asensio, L., Alonso, J., Yustres, Á., Pintado, X., 2014. Multiphysics implementation of advanced soil mechanics models. Comput. Geotech. 60, 20–28. http://dx.doi.org/10.1016/j.compgeo.2014.03.012.

Navarro, V., Asensio, L., De la Morena, G., Pintado, X., Yustres, Á., 2015. Differentiated intra-and inter-aggregate water content models of MX-80 bentonite. Appl. Clay Sci. 118, 325–336. http://dx.doi.org/10.1016/j.clay.2015.10.015.

Navarro, V., Asensio, L., Yustres, Á., De la Morena, G., Pintado, X., 2016. Swelling and mechanical erosion of MX-80 bentonite: pinhole test simulation. Eng. Geol. 202, 99–113. http://dx.doi.org/10.1016/j.enggeo.2016.01.005.

Neretnieks, I., Liu, L., Moreno, L., 2009. Mechanisms and Models for Bentonite Erosion. SKB Technical Report TR-09-35. Svensk Kärnbränslehantering AB. Swedish Nuclear Fuel and Waste Management Co. See:. www.skb.com/publication/1989990/TR-09-35.pdf last accessed March 2017.

Pollock, D.W., 1986. Simulation of fluid flow and energy transport processes associated with high-level radioactive waste disposal in unsaturated alluvium. Water Resour. Res. 22 (5), 765–775. http://dx.doi.org/10.1029/WR022i005p00765.

Quirk, J.P., Schofield, R.K., 1955. The effect of electrolyte concentration on soil permeability. J. Soil Sci. 6 (2), 163–178. http://dx.doi.org/10.1111/j.1365-2389.1955.tb00841.x.

Romero, E., Gens, A., Lloret, A., 1999. Water permeability, water retention and microstructure of unsaturated compacted boom clay. Eng. Geol. 54 (1–2), 117–127. http://dx.doi.org/10.1016/S0013-7952(99)00067-8.

Saiyouri, N., Tessier, D., Hicher, P.Y., 2004. Experimental study of swelling in unsaturated compacted clays. Clay Miner. 39 (4), 469–479. http://dx.doi.org/10.1180/0009855043940148.

Salles, F., Douillard, J.M., Denoyel, R., Bildstein, O., Jullien, M., Beurroies, I., Van Damme, H., 2009. Hydration sequence of swelling clays: evolutions of specific surface area and hydration energy. J. Colloid Interface Sci. 333 (2), 510–522. http://dx.doi.org/10.1016/j.jcis.2009.02.018.

Sane, P., Laurila, T., Olin, M., Koskinen, K., 2013. Current Status of Mechanical Erosion Studies of Bentonite Buffer. Posiva Report 2012-45. Posiva Oy See:. www.posiva.fi/files/3349/POSIVA_2012-45.pdf last accessed March 2017.

Studds, P.G., Stewart, D.I., Cousens, T.W., 1998. The effects of salt solutions on the properties of bentonite-sand mixtures. Clay Miner. 33 (4), 651–660.

Tournassat, C., Appelo, C.A.J., 2011. Modelling approaches for anion-exclusion in compacted Na-bentonite. Geochim. Cosmochim. Acta 75 (13), 3698–3710. http://dx.doi.org/10.1016/j.gca.2011.04.001.

Tournassat, C., Steefel, C.I., Bourg, I.C., Bergaya, F., 2015. Natural and Engineered Clay Barriers. Elsevier.

Wadsö, L., Svennberg, K., Dueck, A., 2004. An experimentally simple method for measuring sorption isotherms. Dry. Technol. 22 (10), 2427–2440. http://dx.doi.org/10.1081/LDRT-200032898.

Wang, L.L., Bornert, M., Yang, D.S., Héripré, E., Chanchole, S., Halphen, B., Pouya, A., Caldemaison, D., 2015. Microstructural insight into the nonlinear swelling of argillaceous rocks. Eng. Geol. 193, 444–453. http://dx.doi.org/10.1016/j.enggeo.2015.05.019.

Yong, R.N., 1999. Soil suction and soil-water potentials in swelling clays in engineered clay barriers. Eng. Geol. 54 (1–2), 3–13. http://dx.doi.org/10.1016/S0013-7952(99)00056-3.

Zhang, F., Low, P.F., Roth, C.B., 1995. Effects of monovalent, exchangeable cations and electrolytes on the relation between swelling pressure and interlayer distance in montmorillonite. J. Colloid Interface Sci. 173 (1), 34–41. http://dx.doi.org/10.1006/jcis.1995.1293.

Zheng, L., Rutqvist, J., Birkholzer, J., Liu, H.H., 2015. On the impact of temperatures up to 200 °C in clay repositories with bentonite engineer barrier systems: a study with coupled thermal, hydrological, chemical, and mechanical modelling. Eng. Geol. 197, 278–295. http://dx.doi.org/10.1016/j.enggeo.2015.08.026.

Zhu, C.M., Ye, W.M., Chen, Y.G., Chen, B., Cui, Y.J., 2013. Influence of salt solutions on the swelling pressure and hydraulic conductivity of compacted GMZ01 bentonite. Eng. Geol. 166, 74–80. http://dx.doi.org/10.1016/j.enggeo.2013.09.001.

Zhu, C.M., Ye, W.M., Chen, Y.G., Chen, B., Cui, Y.C., 2015. Impact of cyclically infiltration of $CaCl_2$ solution and de-ionized water on volume change behavior of compacted GMZ01 bentonite. Eng. Geol. 184, 104–110. http://dx.doi.org/10.1016/j.enggeo.2014.11.005.